Article

Contact Effects on Thermoelectric Properties of Textured Graphene Nanoribbons

David M. T. Kuo [1] and Yia-Chung Chang [2,3,*]

[1] Department of Electrical Engineering and Department of Physics, National Central University, Chungli 320, Taiwan

[2] Research Center for Applied Sciences, Academic Sinica, Taipei 11529, Taiwan

[3] Department of Physics, National Cheng Kung University, Tainan 701, Taiwan

[*] Correspondence: yiachang@gate.sinica.edu.tw

Abstract: The transport and thermoelectric properties of finite textured graphene nanoribbons (t-GNRs) connected to electrodes with various coupling strengths are theoretically studied in the framework of the tight-binding model and Green's function approach. Due to quantum constriction induced by the indented edges, such t-GNRs behave as serially coupled graphene quantum dots (SGQDs). These types of SGQDs can be formed by tailoring zigzag GNRs (ZGNRs) or armchair GNRs (AGNRs). Their bandwidths and gaps can be engineered by varying the size of the quantum dot and the neck width at indented edges. Effects of defects and junction contact on the electrical conductance, Seebeck coefficient, and electron thermal conductance of t-GNRs are calculated. When a defect occurs in the interior site of textured ZGNRs (t-ZGNRs), the maximum power factor within the central gap or near the band edges is found to be insensitive to the defect scattering. Furthermore, we found that SGQDs formed by t-ZGNRs have significantly better electrical power outputs than those of textured ANGRs due to the improved functional shape of the transmission coefficient in t-ZGNRs. With a proper design of contact, the maximum power factor (figure of merit) of t-ZGNRs could reach 90% (95%) of the theoretical limit.

Keywords: textured graphene nanoribbons; topological nature; edge states; junction contact; thermoelectric properties; square-form transmission curve

1. Introduction

Due to global warming, the Kyoto protocol, aiming to reduce CO_2 emissions, was proposed in 1997. Since then, renewable energies including solar, wind, rain, tides, and geothermal heat have become topics of tremendous scientific interest [1]. Thermoelectric devices can be used as power generators and refrigerators. The electrical power based on thermoelectric effects is one of the most important types of green energy [1–6]. Because of the inherent physics of the thermoelectric effect, thermoelectric devices can fully avoid CO_2, hydrofluorocarbon, and perfluorocarbon emissions. In addition, thermoelectric devices can sustain long operation times and avoid mechanical noise.

Recently, energy harvesting applications in nanoscale systems have attracted considerable attention [7–12]. The question of how to obtain the maximum thermoelectric efficiency of heat engines with optimized electrical power output has been a key issue [9–12]. To improve the performance of a heat engine, it is preferable to have the electron transport in the ballistic regime and phonon transport in the diffusive scattering regime. Therefore, a high-performance thermoelectric device needs to provide a channel length shorter than the electron mean free path (λ_e) but much longer than the phonon mean free path (λ_{ph}) in order to reduce the ratio of phonon thermal conductance (κ_{ph}) to electron thermal conductance (κ_e) [13]. It was pointed out in Ref. [9] that a Carnot heat engine favors the electron transport in an energy range where the transmission coefficient has a steep change with respect to energy, e.g., with a square form (SF). Up to now, it remains unclear how to realize

a SF transmission coefficient in realistic thermoelectric devices with a short channel length between thermal contacts [11,14].

Considerable scientific efforts have paved the way to solving such an intriguing problem. Hicks and Dresselhaus theoretically demonstrated that the thermoelectric performance can be significantly enhanced in one-dimensional (1D) nanowires due to the reduced phonon thermal conductance and the enhanced Seebeck coefficient (*S*) [2,3]. According to theoretical modeling, κ_{ph} of 1D silicon quantum dot (QD) superlattices can be reduced by one order of magnitude in comparison with 1D nanowires [7,8]. Due to limitations in technology, the dot-size fluctuation in the 1D silicon quantum dot arrays still remains a serious issue [15,16].

The discovery of graphene in 2004 opened the door to realizing 1D nanowires with a small cross-section to degrade κ_{ph} [17], since one can fabricate graphene nanoribbons (GNRs) with atomic precision via the bottom-up approach [18]. This approach has been successfully applied to build more complex systems, such as armchair GNRs with periodically corrugated edges, called textured AGNRs (t-AGNRs) here [19–25]. The scanning tunneling microscopy (STM) spectra of serially coupled graphene quantum dots (SGQDs) synthesized by t-AGNRs were reported experimentally [25]. Novel graphene-based electronic devices have also focused on AGNRs and t-AGNRs [26]. Recently, the existence of edge states with topological protection in textured zigzag GNRs (t-ZGNRs) has been demonstrated theoretically [27].

Several experimental studies of the thermoelectric properties of graphene-related materials have been reported in recent years [28–34]. Nevertheless, there is a paucity of studies to consider the contact effect on the thermoelectric properties of t-AGNRs and t-ZGNRs [35]. In this work, our goal is to optimize the transmission coefficient of t-GNRs with length shorter than λ_e, but larger than λ_{ph}, under different coupling strengths with the electrical contact. We found that minibands can be formed in these t-GNRs, while their energy gaps can be tuned by varying the size of GQDs and the inter-dot coupling strength. Furthermore, the calculated power factor is very robust against scattering from defects occurring inside the interiors of these t-ZGNRs. The transmission coefficients through the minibands of t-ZGNRs under optimized tunneling rates provide desired characteristics showing a steep change with respect to the energy near the central gap that mimics the theoretical limit obtained by using a SF transmission coefficient. Due to this feature, our calculations reveal that the thermoelectric performance of t-ZGNRs can be significantly better than that of t-AGNRs. The maximum power factor (figure of merit) of t-ZGNRs could reach 90% (95%) of that obtained with the SF transmission coefficient. Therefore, the t-ZGNR is a promising candidate for applications in nanoscale energy harvesting.

2. Calculation Methods

To model the thermoelectric properties of t-GNRs connected to the electrodes, it is a good approximation to employ a tight-binding model with one p_z orbital per atomic site to describe the electronic states [36–40]. The Hamiltonian of the nano-junction system depicted in Figure 1, including four different GNR structures, can be written as $H = H_0 + H_{GNR}$ [41], where

$$
\begin{aligned}
H_0 &= \sum_k \epsilon_k a_k^\dagger a_k + \sum_k \epsilon_k b_k^\dagger b_k \\
&+ \sum_\ell \sum_k V_{k,\ell,j}^L d_{\ell,j}^\dagger a_k + \sum_\ell \sum_k V_{k,\ell,j}^R d_{\ell,j}^\dagger b_k + h.c.
\end{aligned}
\tag{1}
$$

The first two terms of Equation (1) describe the free electrons in the left (*L*) and right (*R*) electrodes. $a_k^\dagger$ ($b_k^\dagger$) creates an electron with wave number *k* and energy ϵ_k in the left (right) electrode. $V_{k,\ell,j=1}^L$ ($V_{k,\ell,j=N_z(N_a)}^R$) describes the coupling between the left (right) lead with its adjacent atom in the ℓ-th row.

$$
H_{GNR} = \sum_{\ell,j} E_{\ell,j} d_{\ell,j}^\dagger d_{\ell,j} - \sum_{\ell,j} \sum_{\ell',j'} t_{(\ell,j),(\ell',j')} d_{\ell,j}^\dagger d_{\ell',j'} + h.c,
\tag{2}
$$

where $E_{\ell,j}$ is the on-site energy for the p_z orbital in the ℓ-th row and j-th column. Here, the spin-orbit interaction is neglected. $d^\dagger_{\ell,j}(d_{\ell,j})$ creates (destroys) one electron at the atom site labeled by (ℓ,j), where ℓ and j, respectively, are the row and column indices as illustrated in Figure 1. $t_{(\ell,j),(\ell',j')}$ describes the electron hopping energy from site (ℓ,j) to site (ℓ',j'). The tight-binding parameter used for GNRs is $E_{\ell,j} = 0$ for the on-site energy and $t_{(\ell,j),(\ell',j')} = t_{pp\pi} = 2.7$ eV for the nearest-neighbor hopping strength.
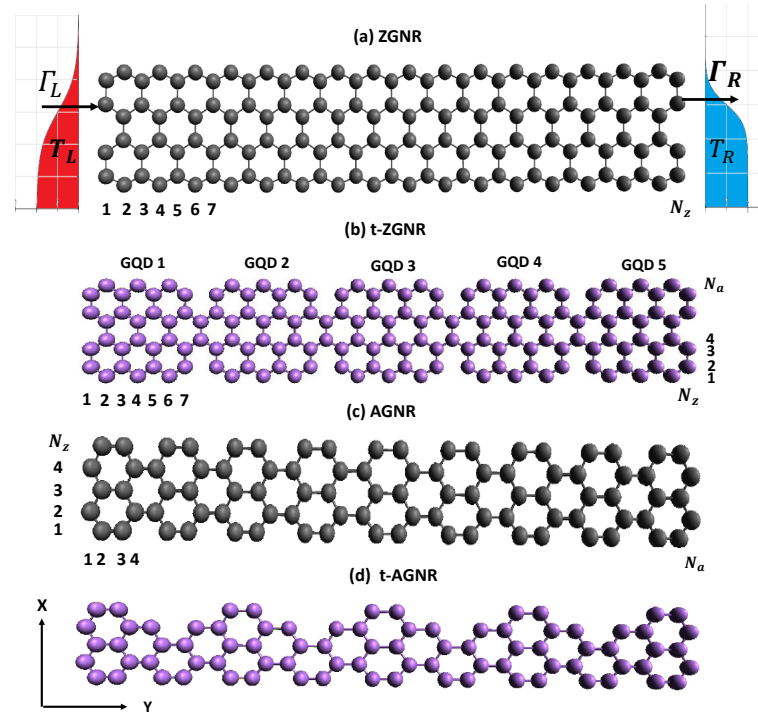

Figure 1. Schematic diagrams of (**a**) ZGNR, (**b**) textured-ZGNR (t-ZGNR), (**c**) AGNR, and (**d**) t-AGNR. In (**a**), we also show the electrodes with Γ_L (Γ_R) denoting the tunneling rate of the electrons between the left (right) electrode and the leftmost (rightmost) atoms of the ZGNR. T_L and T_R denote the temperature of the left (L) and the right (R) electrodes, respectively. Note that t-ZGNRs can be formed by periodically removing some carbon atoms on the zigzag edges of ZGNRs. In (**b**), the t-ZGNR consists of GQDs with size characterized by $(N_a, N_z) = (8,7)$. In (**c**), the AGNR has a length $N_a = 36$ and width $N_z = 5$. In (**d**), the width and length of the unit cell for the t-AGNR superlattice are characterized by $N_z = 5$ and $N_a = 8$, respectively.

To study the transport properties of a GNR junction connected to electrodes, it is convenient to use the Keldysh Green function technique [41]. Electron and heat currents leaving the electrodes can be expressed as

$$J = \frac{2e}{h} \int d\varepsilon\, \mathcal{T}_{LR}(\varepsilon)[f_L(\varepsilon) - f_R(\varepsilon)], \tag{3}$$

and

$$Q_{e,L(R)} = \frac{\pm 2}{h} \int d\varepsilon\, \mathcal{T}_{LR}(\varepsilon)(\varepsilon - \mu_{L(R)})[f_L(\varepsilon) - f_R(\varepsilon)] \tag{4}$$

where $f_\alpha(\varepsilon) = 1/\{\exp[(\varepsilon - \mu_\alpha)/k_B T_\alpha] + 1\}$ denotes the Fermi distribution function for the α electrode, where μ_α and T_α are the chemical potential and the temperature of the α electrode. e, h, and k_B denote the electron charge, the Planck constant, and the Boltzmann constant, respectively. $\mathcal{T}_{LR}(\varepsilon)$ denotes the transmission coefficient of a GNR connected to electrodes, which can be solved by the formula $\mathcal{T}_{LR}(\varepsilon) = 4Tr[\Gamma_L(\varepsilon)G^r(\varepsilon)\Gamma_R(\varepsilon)G^a(\varepsilon)]$ [42,43], where $\Gamma_L(\varepsilon)$ and $\Gamma_R(\varepsilon)$ denote the tunneling rate (in energy units) at the left and right leads, and

$G^r(\varepsilon)$ and $G^a(\varepsilon)$ are the retarded and advanced Green's functions of the GNR, respectively. The tunneling rates are described by the imaginary part of the self-energy correction on the interface atoms of the GNR due to the coupling with nearby atoms in the adjacent electrodes, i.e., $\Gamma_{L(R)}(\varepsilon) = -Im(\Sigma^r_{L(R)}(\varepsilon))$. Such coupling depends on the contact quality with the electrodes, which is characterized by the interaction strength $V^L_{k,\ell,j=1}(V^R_{k,\ell,j=N_z(N_a)})$ with the left (right) lead. Here, we have adopted energy-independent tunneling rates $\Gamma_{L(R)}(\varepsilon) = \Gamma_{L(R)}$, which is reasonable in the wide-band limit for the electrodes [42]. Note that Γ_α and Green's functions are matrices in the basis of tight-binding orbitals. Γ_α for the boundary atoms have diagonal entries given by the same constant Γ_t. Because of the line contact, as illustrated in Figure 1, the contact resistance can be much smaller than that of surface contact [44]. Meanwhile, the variation of tunneling rates could reveal different contact properties, such as the Schottky or ohmic contact [45].

In the linear response regime, the electrical conductance (G_e), Seebeck coefficient (S), and electron thermal conductance (κ_e) are given by $G_e = e^2\mathcal{L}_0$, $S = -\mathcal{L}_1/(eT\mathcal{L}_0)$, and $\kappa_e = \frac{1}{T}(\mathcal{L}_2 - \mathcal{L}_1^2/\mathcal{L}_0)$, with $\mathcal{L}_n (= 0, 1, 2)$ defined as

$$\mathcal{L}_n = \frac{2}{h} \int d\varepsilon \, \mathcal{T}_{LR}(\varepsilon)(\varepsilon - \mu)^n \frac{\partial f(\varepsilon)}{\partial \mu}. \tag{5}$$

Here, $f(\varepsilon) = 1/(exp^{(\varepsilon-\mu)/k_BT} + 1)$ is the Fermi distribution function of electrodes at equilibrium temperature T and chemical potential μ. As seen in Equation (5), the transmission coefficient $\mathcal{T}_{LR}(\varepsilon)$ plays a significant role for electron transport between the left (L) and right (R) electrodes. At zero temperature, the electrical conductance is given by $G_e(\mu) = \frac{2e^2}{h} \mathcal{T}_{LR}(\mu)$. In the current study, only even numbers of N_a are considered, to avoid unwanted dangling-bond states. We have developed an efficient computation method that allows us to calculate the non-equilibrium Green's functions of large-sized quantum structures. For the current study, textured ZGNRs and AGNRs with lengths up to 14 nm are considered.

3. Results and Discussion

3.1. Graphene Nanoribbons

Topological states offer promising applications in electronics and optoelectronics, owing to their robustness in transport characteristics against defect scattering. Many studies have confirmed that 2D and 1D topological states (TSs) exist in certain material structures [46–51]. For instance, there exists a 2D topologically protected interface state in HgTe/CdTe superlattices [46,47]. One-dimensional (1D) TSs were theoretically predicted to exist in square selenene and tellurene [51]. Recently, zero-dimensional (0D) TSs of finite-size GNRs have been extensively studied [19–25] because the 0D TS offers more flexibility in the design of complicated electronic circuits [22]. Before illustrating electron-coherent transport through SGQDs formed by t-ZGNRs, we first examine the characteristics of 0D TSs of finite-size GNRs by calculating their transmission coefficient, $\mathcal{T}_{LR}(\varepsilon)$.

Figure 2 shows the calculated electron conductance, G_e, at $k_BT = 0$ as a function of μ for various N_a with $N_z = 7$. We note that there are two zigzag edge states localized at the top and bottom sides of the GQDs depicted in Figure 1a. For $N_a = 40$, their wave functions are well separated along the armchair direction [37]. The electrical conductance spectrum shows that $G_e = 2G_0$ at $\mu = 0$ and $G_e = G_0$ for other electronic states, where $G_0 = \frac{2e^2}{h}$ is the quantum conductance. Such zero energy modes were observed experimentally by STM [23]. When two electronic states are closely spaced (with energy separation less than the broadening), G_e can become larger than G_0. As N_a decreases, G_e for the zero-energy mode is split into two peaks corresponding to the bonding and antibonding states of coupled zigzag edge states, as seen in Figure 2c. When $N_a = 12$, these two peaks are well separated. Here, ϵ_{HO} and ϵ_{LU} denote the energy levels of the highest occupied molecular orbital (HOMO) and the lowest unoccupied molecular orbital (LUMO), respectively. Due to the short decay lengths along the armchair edge directions for zigzag edge states, $\mathcal{T}_{LR}(\varepsilon)$

of Σ_0 also depends on whether the zigzag or armchair edges are coupled to the electrodes. In Ref. [52], it is proposed that a single QD can be used to realize a Carnot heat engine. However, the channel length for $N_z = 7$ ($L_z = 0.738$ nm) is too small to avoid the serious degradation of the figure of merit due to the phonon heat conductivity, κ_{ph}. On the other hand, for the large N_z case ($N_z \gg N_a$), a finite GNR shows metallic behavior, leading to unfavorable thermoelectric properties. To maintain a sizable gap ($10 k_B T$) around the charge neutrality point (CNP) while keeping κ_{ph} small enough to preserve a decent figure of merit ($ZT = \frac{S^2 G_e T}{\kappa_e + \kappa_{ph}}$), t-ZGNR becomes a suitable candidate, as we shall discuss below.
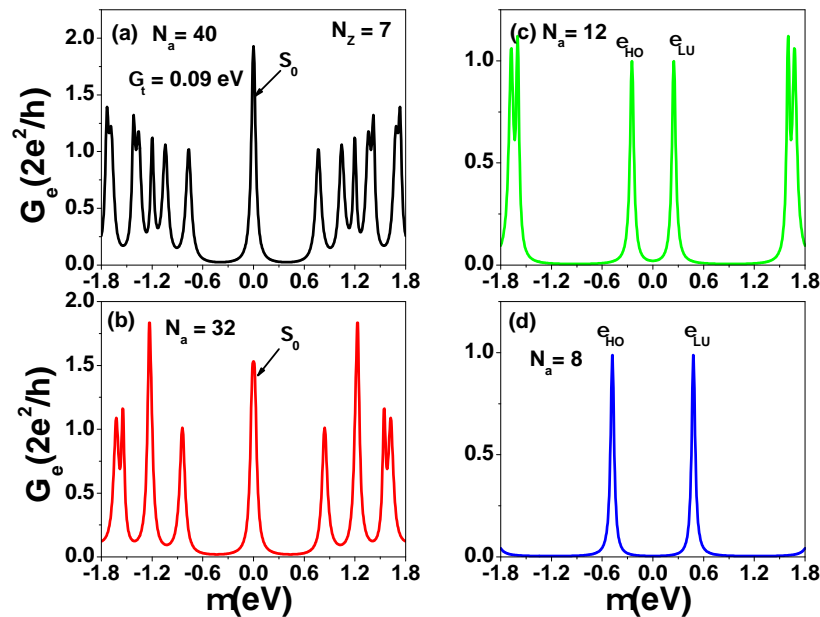

Figure 2. Electrical conductance, G_e, of a finite GNR with armchair edges coupled to the electrodes at $k_B T = 0$ as a function of the chemical potential, μ, for various widths with (**a**) $N_a = 40$, (**b**) $N_a = 32$, (**c**) $N_a = 12$, and (**d**) $N_a = 8$. N_z is fixed at 7. Here, we have adopted an electron tunneling rate, $\Gamma_t = 90$ meV.

3.2. SGQDs Formed by Textured ZGNRs

For energy harvesting applications at room temperature, we need to design a $\mathcal{T}_{LR}(\varepsilon)$ spectrum with a square shape near the central gap to obtain optimized ZT and electrical power output [9]. Let us consider an SGQD formed by t-ZGNR. A t-ZGNR can be realized by tailoring a GNR with periodic indentation on the zigzag edges, such as the structure shown in Figure 1b. This t-ZGNR consists of GQDs with size characterized by $N_a = 12$ and $N_z = 7$. A single GQD of this size has resonance energies $\varepsilon_{LU(HO)} = \pm 0.247$ eV near the CNP, as shown in Figure 2c. For two coupled GQDs (2GQDs), there is one satellite peak on the left (right) side of the $\varepsilon_{HO(LU)}$ peak (see Figure 3b). For six coupled GQDs (6GQDs), we have five additional peaks with $\varepsilon_{e(h),1} = \pm 0.3105$ eV, $\varepsilon_{e(h),2} = \pm 0.468$ eV, $\varepsilon_{e(h),3} = \pm 0.6705$ eV, $\varepsilon_{e(h),4} = \pm 0.882$ eV, and $\varepsilon_{e(h),5} = \pm 1.0665$ eV on the right (left) side of $\varepsilon_{LU(HO)} = \pm 0.247$ eV (see Figure 3f). We note that $G_e(\mu)$ is fully suppressed for μ between ε_{HO} and ε_{LU}. Therefore, SGQDs formed by t-ZGNRs function as filters to block electrons with energies near the CNP, which is different from that of serially coupled antidots realized by ZGNRs with nanopores [53]. The separation between peaks is inhomogeneous. In addition, the ε_{HO} and ε_{LU} peaks become sharper with increasing GQD number. These features are attributed to a special parity symmetry in the supercell of ZGNRs. Due to the coupling of transverse and longitudinal wave numbers in ZGNRs, the density distributions of the electronic state near CNP are inhomogeneous [54]. AGNRs do not have such a parity in the supercell. The feature provides a significant effect on the transmission coefficient of SGQDs formed by t-ZGNRs. To further illustrate the characteristics of the edge states,

we show the charge densities of states with ε_{LU}, $\varepsilon_{e,1}$, and $\varepsilon_{e,2}$ for the case of 6GQDs in Figure A1 of Appendix A.
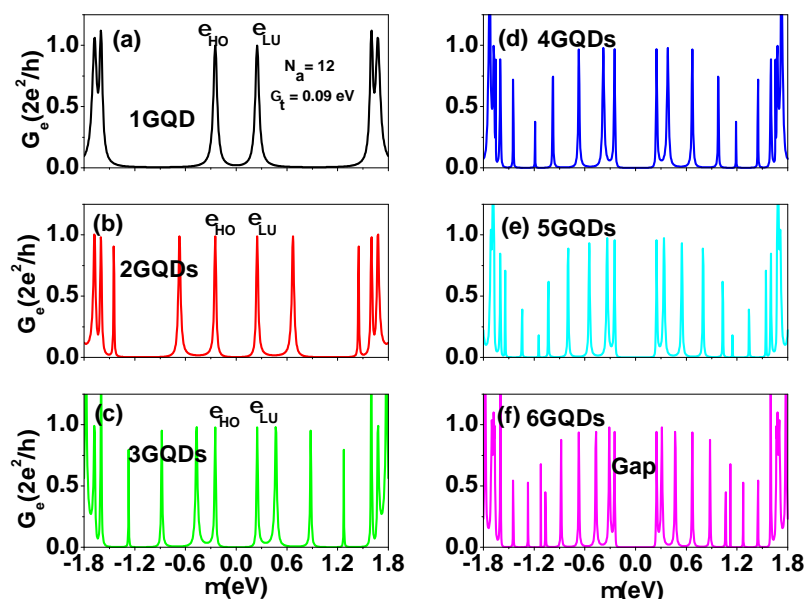

Figure 3. Electrical conductance, G_e, as a function of μ for SGQDs with GQD numbers, $n = 1, 2, 3, 4, 5$, and 6 in subfigures (**a**) 1GQD, (**b**) 2GQDs, (**c**) 3GQDs, (**d**) 4GQDs, (**e**) 5GQDs, and (**f**) 6GQDs, respectively. The size of each GQD in these SGQDs is characterized by $N_a = 12$ and $N_z = 7$. Other physical parameters are the same as those used in Figure 2c.

Previous theoretical studies have demonstrated that edge defects can significantly reduce the electron quantum conductance of ZGNRs [55,56]. Here, we investigate how defects (either at the edge or in the interior region) influence the thermoelectric characteristics of t-ZGNRs by introducing energy shifts $\Delta_{\ell,j}$ on designated defect sites. $\Delta_{\ell,j}$ could be positive or negative, which depends on the type of defect [56]. To model a vacancy within a tight binding model, one typically takes $\Delta_{\ell,j} \to \infty$. The larger the orbital energy shift, the stronger the effect on the electrical conductance [57]. Here, we consider the case of a positive and large Δ to investigate the effects of defects on the electron transport of t-ZGNRs. We calculate G_e, κ_e, S, and power factor $PF = S^2 G_e$ for different defect locations for the case of 15 GQDs ($L_z = 14.5$ nm or $N_z = 119$) with $\Gamma_t = 0.54$ eV and show the results in Figure 4.

As seen in Figure 4a,b, the size of the central gap and the shape of G_e and κ_e spectra (green lines) are changed only slightly when the defects are located in the interior region. However, the G_e and κ_e values near the central gap become seriously suppressed (as shown by red lines) when a single defect is located at a zigzag edge site labeled by $(1, 4)$, where the charge density of the $\varepsilon_{LU(HO)}$ electronic state is peaked. As seen in Figure 4c, the antisymmetric pattern of the Seebeck coefficient $S(\mu)$ (with respect to the sign change of μ) due to the electron–hole symmetry is distorted in the presence of defects. The peak value of the power factor $PF = S^2 G_e$ near the central gap is seriously reduced when defects occur on the edge, but much less affected by defects in the interior region, as illustrated in Figure 4d. Here, and henceforth, κ_e is in units of $\kappa_0 = 0.62$ nW/K, S is expressed in units of $k_B/e = 86.25$ µV/K, and the power factor (PF) in units of $2k_B^2/h = 0.575$ pW/K^2. It is remarkable to see that PF is very robust against defect scattering when defects are away from zigzag edges. Such location-dependent effects can be depicted by the charge density distribution in Figure A1. To reduce the defect effect on electron transport, one needs to avoid creating defects randomly located on the zigzag edges.
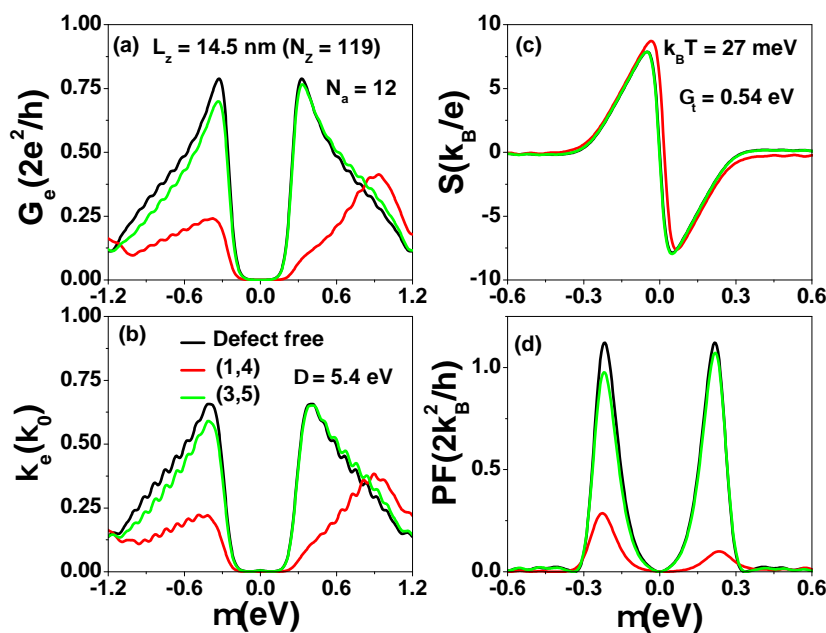
Figure 4. (**a**) Electrical conductance G_e, (**b**) electron thermal conductance κ_e, (**c**) Seebeck coefficient S, and (**d**) power factor $PF = S^2 G_e$ as functions of μ for defect locations at $k_B T = 27$ meV. The tunneling rates used are $\Gamma_t = 0.54$ eV. The length of SGQD is $L_z = 14.5$ nm ($N_z = 119$). Each GQD in the SGQD structure has size $N_a = 12$ and $N_z = 7$.

We note that SGQDs are formed by periodically removing some carbon atoms on the zigzag edges of ZGNRs. To understand the relationship between the quantum states near the central gap in the SGQD formed by t-ZGNRs and the quantum states near the zero energy modes of ZGNRs, we show a comparison of the subband structures of the infinitely long t-ZGNR shown in Figure 1b and unaltered ZGNR shown in Figure 1a (with an enlarged supercell of length $L = 4a$ to match the unit cell of t-ZGNR) in Figure A2a of the Appendix A. Note that the first Brillouin zone (BZ) has one quarter the size of the BZ of ZGNR. Thus, the subband structures shown in Figure A2a include the zone-folding effect that maps the zone boundary ($k_z = \pi/a$) of the unfolded BZ of ZGNR to $k_z = 0$ of the folded BZ here. As expected, the unaltered ZGNR has edge states with zero energy for $k_z < 0.06\, \pi/a = 0.24\, \pi/L$. The two edge states are strongly coupled in the t-ZGNR, with energy splitting of 2.5 eV. On the other hand, the edge states at the mini-zone boundary ($k_z = \pi/L$) with energies corresponding to the HOMO (LUMO) level are nearly unaffected by the removal of a carbon atom in the neck region of t-ZGNR, since the wave functions of these edge states have a node at that position. Theoretical calculations of the Zak phases of various t-ZGNRs indicate that the topological nature of the edge states of t-ZGNRs is preserved even though their energy levels are shifted away from the CNP [27]. Thus, the transport through these states should be rather insensitive to the presence of defects inside the t-ZGNR.

Junction tunneling rates can be affected by the quality of contact between the electrode and semiconductor [44], which is a critical issue for device applications of two-dimensional materials [58]. To clarify the contact effect, we show in Figure 5 the calculated G_e, κ_e, S, and ZT at room temperature for various tunneling rates (Γ_t) for a t-ZGNR with 15 GQDs, each having the dimension $N_a = 8$ and $N_z = 7$, as shown in Figure 1b. When the tunneling rate increases, the transmission coefficient $\mathcal{T}_{LR}(\epsilon)$ through minibands close to HOMO (LUMO) is enhanced. For the case of 15 GQDs, there are 15 peaks in each miniband (see Figure A3). Such an enhancement leads to an increase in both G_e and κ_e, as seen in Figure 5a,b. However, S is essentially independent of the variation in Γ_t, as indicated by the collapsing of all four curves in Figure 5c. As a result, the power factor $PF = S^2 G_e$ also increases with Γ_t. It is noted that the maximum S reaches 1.51 mV/K (see Figure 5c), which is much larger than

that observed experimentally in gapless graphene [28,29]. In Figure 5d, the maximum ZT occurs at $\mu = \pm0.423$ eV, where $\kappa_{ph} \gg \kappa_e$. Therefore, the enhancement in ZT with respect to the increase in Γ_t mainly arises from the enhancement in PF. Here, we have included the effect of phonon thermal conductance, κ_{ph}, and assumed $\kappa_{ph} = F_s\kappa_{ph}^0$ in the calculation of ZT in Figure 5d, where $\kappa_{ph}^0 = \frac{\pi^2 k_B^2 T}{3h}$ is the phonon thermal conductance of an ideal ZGNR. We adopt the room-temperature value of $\kappa_{ph}^0 = 0.285$ nW/K for the ZGNR with width $N_a \leq 8$ obtained by a first-principles calculation as given in Ref. [59]. $F_s = 0.1$ denotes a reduction factor resulting from quantum constriction in t-ZGNRs. It has been theoretically demonstrated that the magnitude of κ_{ph} can be reduced by one order magnitude for ZGNRs with "edge vacancies" [60], which is similar to the mechanism introduced in silicon nanowires with surface roughness [61]. The measured λ_{ph} can be reduced from 300–600 nm in a single layer graphene to 10 nm in graphene nanostructures (see [30] and references therein). Recently, a very short λ_{ph} has been reported experimentally, which offers promise for enhancing the figure of merit (ZT) of graphene heterostructures [31–34].
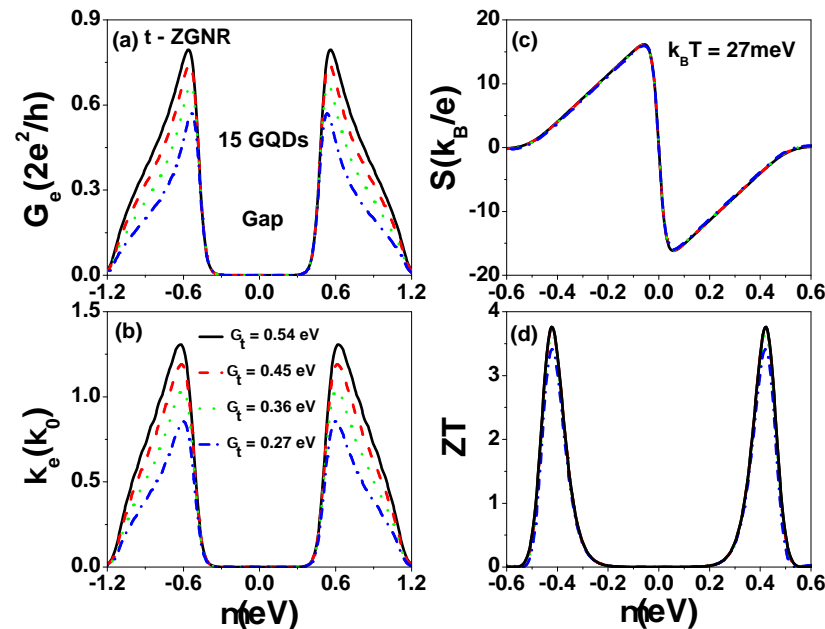

Figure 5. (**a**) Electrical conductance G_e, (**b**) electron thermal conductance κ_e, (**c**) Seebeck coefficient S, and (**d**) figure of merit ZT as functions of μ for various tunneling rates (Γ_t) at $k_B T = 27$ meV. The t-ZGNR structure with $L_z = 14.5$ nm considered is illustrated in Figure 1b. The size of each GQD in the t-ZGNR is characterized by $N_a = 8$ and $N_z = 7$.

The calculated results shown in Figure 5 imply that $ZT > 3$ could be realized by using SGQDs formed by t-ZGNRs for tunneling rates corresponding to Γ_t between $t_{pp\pi}/10(0.27$ eV) and $t_{pp\pi}/5(0.54$ eV). In Figure A3 of Appendix A, we show the peak value of $ZT(ZT_{max})$ as a function of tunneling rate Γ_t, and we found that the ZT_{max} can be larger than 3 for Γ_t between 0.18 eV and 1.45 eV. We note that if a semi-infinite ZGNR contact is used, it is reasonable to assume that the coupling strength between the semi-infinite ZGNR and t-ZGNR can be comparable to the hopping strength $t_{pp\pi} = 2.7$ eV. Here, we show that the maximum ZT can reach 3.7 with $\Gamma_t = 0.54$ eV $= t_{pp\pi}/5$, which could be achievable with good contact.

Because S is a robust physical quantity with respect to the variation in tunneling rate and channel length (which only depend on the magnitude of the central gap and temperature in our case), the optimization of G_e becomes a critical issue in SGQDs when $\kappa_{ph} \gg \kappa_e$. To provide a better understanding of the effect of the tunneling rate on the thermoelectric properties, we further investigate the relation between the tunneling rate

and the spectral shape of $\mathcal{T}_{LR}(\varepsilon)$. In Figure 6, we show a comparison of the tunneling spectra, $\mathcal{T}_{LR}(\varepsilon)$, of a t-ZGNR with 15 GQDs calculated for two different tunneling strengths, $\Gamma_t = 0.54$ eV and $\Gamma_t = t_{pp\pi} = 2.7$ eV. In Figure 6a, the area below the $\mathcal{T}_{LR}(\varepsilon)$ curve shows a right-triangle shape that has a steep change with respect to ε on the side toward the central gap. In Figure 6b (with $\Gamma_t = t_{pp\pi} = 2.7$ eV), the electron tunneling probability through the electronic states near $\varepsilon_{LU(HO)}$ is highly suppressed, leading to an arch-like area under the $\mathcal{T}_{LR}(\varepsilon)$ curve. The corresponding maximum ZT for this case is 2.3, which is much smaller than that of Figure 5d. The results of Figure 6a,b indicate that the shape of the area under the $\mathcal{T}_{LR}(\varepsilon)$ curve depends on the tunneling rate (or the quality of contact). An arch-like area under $\mathcal{T}_{LR}(\varepsilon)$ will reduce the electrical conductance G_e near the central gap.
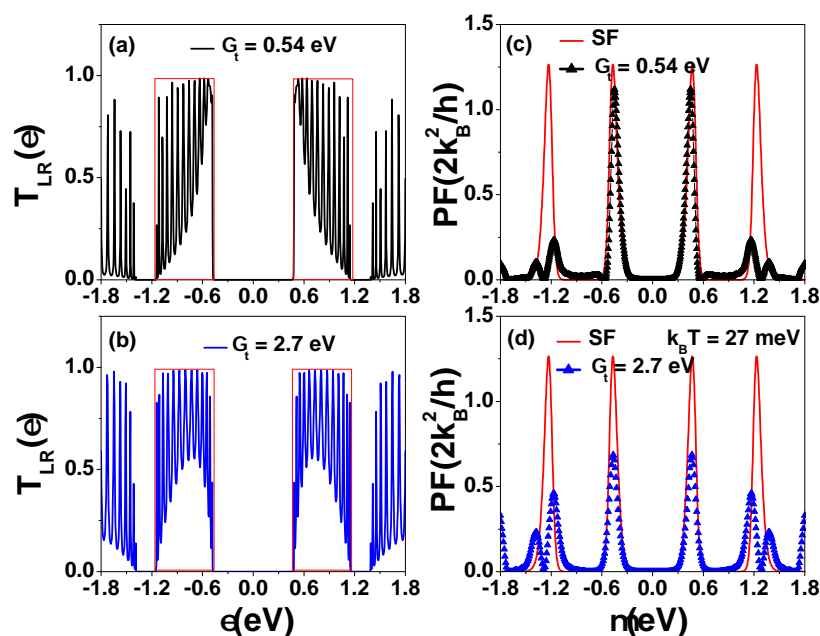

Figure 6. (**a**,**b**) Transmission coefficients $\mathcal{T}_{LR}(\varepsilon)$ as functions of energy for a t-ZGNR with $\Gamma_t = 0.54$ eV and $\Gamma_t = 2.7$ eV. The $\mathcal{T}_{LR}(\varepsilon)$ with square form (SF) is also plotted by a curve with red color. (**c**,**d**) Power factor as functions of μ for two tunneling rates at $k_B T = 27$ meV. Other physical parameters are the same as those used in Figure 5.

As seen in Figure 6c, the optimized PF found near $\Gamma_t = 0.54$ eV is very close to that obtained by using an ideal SF transmission spectrum (indicated by the red line), which exhibits the quantum limit of power factor for 1D systems with $PF_{QB} = 1.2659(\frac{2k_B^2}{h})$ [9,11]. We obtain the optimized $PF_{max} = 0.9\ PF_{QB}$, which is the same as that of the quantum interference heat engine [62]. This analysis suggests that using SGQDs with suitable tunneling rates could achieve performance close to an optimum heat engine with maximum electrical power output and high thermoelectric efficiency. With the same κ_{ph}, the ZT_{max} of t-ZGNRs can reach 95% of that obtained by an SF transmission coefficient (with $ZT_{max} = 3.951$). Thus far, we have only considered periodically indented structures on both the top and bottom zigzag edges (see Figure 1b). We note that the same optimized result of $PF_{max} = 0.9\ PF_{QB}$ can also be achieved in periodically indented structures corresponding to Figure 6 but with a textured pattern only on one zigzag side, provided that the tunneling rate can be increased to $\Gamma_t = 0.72$ eV. The results are shown in Figure A3 of Appendix A.

3.3. Armchair Graphene Nanoribbons

As shown in Figures 5 and 6, SGQDs formed by metallic ZGNRs can become semiconductors. Next, we investigate whether their thermoelectric performance is better than that of AGNRs or t-AGNRs. We note that many designs have focused on the optimization of the thermoelectric performance of AGNRs [63–66]. Here, we first consider AGNRs with their

zigzag ends coupled to electrodes, as depicted in Figure 1c. Figure 7 shows the calculated transmission coefficient $\mathcal{T}_{LR}(\epsilon)$ for different defect locations with $N_z = 7$, $N_a = 100$ and $\Delta = 5.4$ eV. We choose $\Gamma_t = 2.7$ eV, which gives the optimized shape of the transmission coefficient in a defect-free situation in Figure 7a. For finite-size AGNRs, the conduction (valence) subband states are quantized, leading to closely spaced peaks with staircase-like structures, as revealed by the $\mathcal{T}_{LR}(\varepsilon)$ spectrum. The area under the $\mathcal{T}_{LR}(\varepsilon)$ curve for states derived from the first subband has a parabolic shape, which does not meet the criterion for achieving an optimized thermoelectric property. For a single defect at edge location (1,3), all but the transmission coefficient spectrum of the first conduction subband are affected significantly. When the defect is located at site (3,3), the spectra for the first conduction subband and the first valence subband are nearly unaffected. Nevertheless, when the defect occurs at (4,4) the spectra in these two subbands show a remarkable change. In the current studies, we do not observe the Anderson localization effect, which leads to a vanishing G_e in the subband regions when a single defect occurs on the edges of ZGNRs and AGNRs [67]. This implies that the GNRs considered are not exact 1D systems.
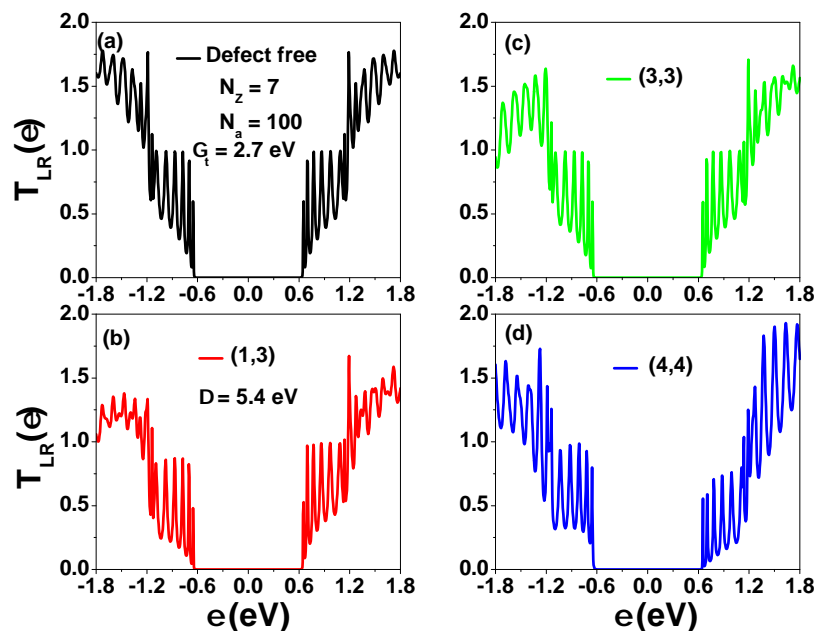

Figure 7. Transmission coefficient of AGNRs as a function of ε for $\Gamma_t = 2.7$ eV, $N_z = 7$, and $N_a = 100$ ($L_a = 10.5$ nm) with (**a**) no defect, (**b**) a defect at site (1,3), (**c**) a defect at site (3,3), and (**d**) a defect at site (4,4). The energy shift at a defect site adopted is $\Delta = 5.4$ eV.

To illustrate the effects of defects on the thermoelectric properties of finite AGNRs, we show the calculated electrical conductance (G_e), Seebeck coefficient (S), power factor (PF), and figure of merit (ZT) as functions of μ at $k_B T = 27$ meV in Figure 8. The four curves in each diagram correspond to the effects of defects located at the four sites considered in Figure 7. As seen in Figure 8a, the spectra of G_e for defects at locations (1,3) and (4,4) are degraded seriously, either in the valence subband or conduction subband, producing highly asymmetrical behavior in electron transport. Due to the robustness of the Seebeck coefficient in the central gap region, the effect of defects on the power factor is solely determined by G_e. Although the maximum S is larger than that of Figure 5c due to the larger gap in AGNRs with $N_z = 7$, the PF values are smaller than the corresponding values of the optimized t-ZGNR shown in Figure 6 (with $\Gamma_t = 0.54$ eV). This is mainly attributed to the different shapes in the area under the transmission coefficient curve. As a consequence, the G_e in AGNRs resulting from thermionic tunneling effects is less favorable. Note that we have adopted $\kappa_{ph} = 0.0285$ nW/K [59] in Figure 8d, which is the same as the κ_{ph} used in Figure 5d.
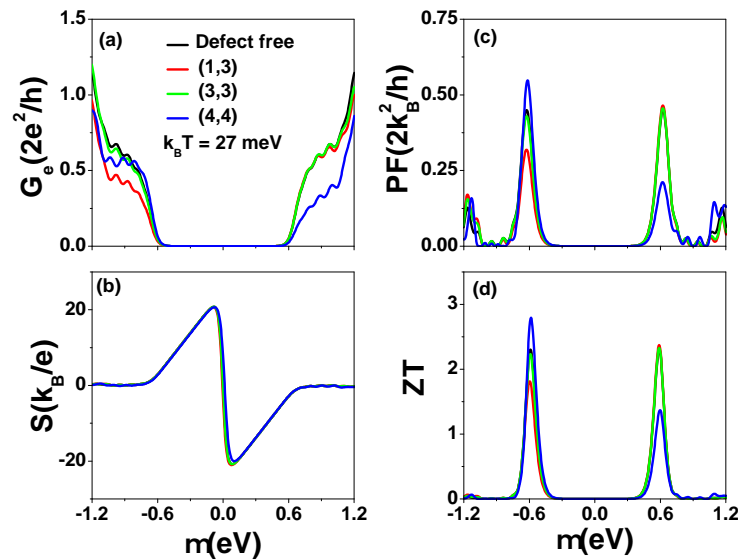
Figure 8. (**a**) Electrical conductance G_e, (**b**) Seebeck coefficient S, (**c**) power factor PF, and (**d**) figure of merit ZT as functions of μ for different defect locations at $k_B T = 27$ meV. Other physical parameters are the same as those of Figure 7. The phonon thermal conductance (κ_{ph}) considered is the same as that used in Figure 5 ($\kappa_{ph} = 0.0285$ nW/K).

3.4. SGQDs Formed by Textured AGNRs

Finally, we study the thermoelectric effect of SGQD structures based on the t-AGNR structure, as shown in Figure 1d. The electronic structures and density of states (DOS) of t-AGNR superlattices have been studied theoretically by using density functional theory (DFT) [21,40]. Electronic structures of t-AGNRs can also be calculated by using a tight-binding model, and results are in good agreement with the DFT calculation [40]. Figure 9 shows the calculated $\mathcal{T}_{LR}(\varepsilon)$ of SGQD junctions made from t-AGNRs as functions of ε for three different N_a values with N_z fixed at 5. We adopt the optimized tunneling rate with $\Gamma_t = 2.7$ eV. Although the AGNR with $N_z = 5$ is metallic, the textured AGNR can be semiconducting, as illustrated by the sizable central gap (1.098 eV) in Figure 9. In Figure A2b of Appendix A, we show a comparison of the subband structures of the t-AGNR and unaltered AGNR (with an enlarged supercell of length $L = 2a'$ to match the unit cell of t-AGNR), where $a' = \sqrt{3}a$ is the unit cell length of the AGNR. We see that the two subbands with linear dispersion in the metallic $N_z = 5$ AGNR are split into two subbands with parabolic dispersion near zero wave number once the quantum constriction takes effect in the t-AGNR. It is worth noting that edge states with zero energy can exist at the left and right ends (with zigzag edges) of the truncated t-AGNR in contact with electrodes. These edge states can contribute to $\mathcal{T}_{LR}(\varepsilon)$ for t-AGNRs with a short SGQD structure (see Figure A4 in Appendix A), since their wave functions decay exponentially along the armchair direction. The area under the $\mathcal{T}_{LR}(\varepsilon)$ curve has an arch-like shape that does not change much as we vary the tunneling rate.

Figure 10 shows the calculated G_e, S, PF, and ZT of SGQD junctions made from a t-AGNR with $N_z = 5$ and $N_a = 132$ ($N_{QD} = 15$) as functions of temperature for different μ values. Solid and dashed lines correspond to $\mu = 0.52$ eV and $\mu = 0.36$ eV, respectively. The first conduction subband edge occurs at $\mu_{edge} = 0.544$ eV. At a given temperature $k_B T = 27$ meV, the maximum power factor occurs at $\mu = 0.52$ eV. For $\mu = 0.36$ eV, which is far away from μ_{edge}; the calculated G_e in the thermionic-assisted tunneling process (TATP) is extremely small, whereas its Seebeck coefficient is highly enhanced. The temperature-dependent S for this case is complicated. Its temperature dependence can be described by three different functions in three temperature ranges, as illustrated in Figure 10b. In region one ($T < 90$ K), we have $S_1 = -\frac{\pi^2 k_B^2 T}{3e} \frac{\partial ln(\mathcal{T}_{LR}(\varepsilon))}{\partial \varepsilon}|_{\varepsilon=\mu}$. In region three ($T > 120$ K), we have $S_3 = \frac{\mu - \mu_{edge}}{eT}$ [68]. In region two, the analytic expression of S_2 is unknown. In TATP, G_e can

be described by the expression $exp^{(\mu-\mu_{edge})/(k_B T)}$. As a consequence, the power factor and figure of merit are small for $\mu = 0.36$ eV. When $\mu = 0.52$ eV, the PF is enhanced quickly in the range 50 K $< T <$ 120 K. Within this temperature region, ZT shows a similar behavior of PF. When $T > 120$ K, the temperature-dependent ZT has the same trend of S because the heat current is dominated by the linear-T phonon thermal conductance $\kappa_{ph} = F_s \frac{\pi^2 k_B^2 T}{3h}$, which cancels out the factor of TG_e in the numerator of ZT. It is worth noting that the optimized PF of t-AGNRs at $T = 325$ K is only one half of the power factor of the t-ZGNR shown in Figure 6c.
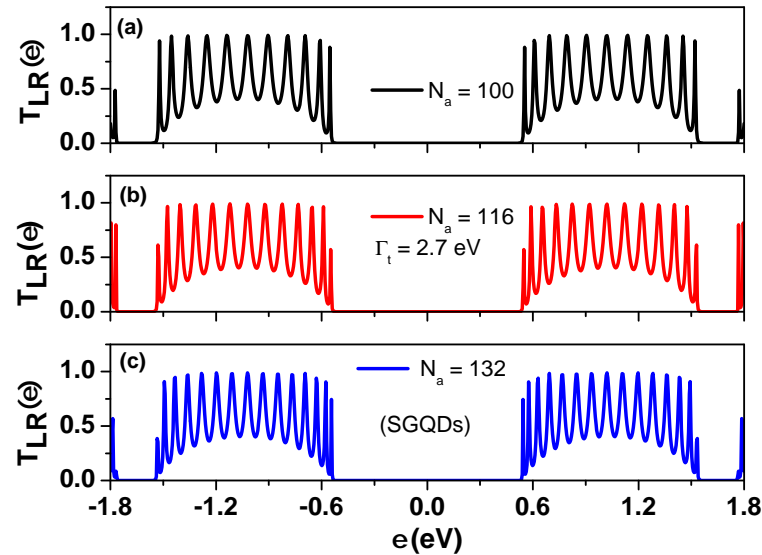

Figure 9. Transmission coefficient of SGQD with $N_z = 5$ for various N_a values as a function of energy ε. $\Gamma_t = 2.7$ eV. Here, $N_a = 12 + 8 \times N_{QD}$, where N_{QD} is the number of GQDs in the interior region of the structure, and they are sandwiched between two smaller GQDs of $N_a = 6$ connected to electrodes. In (**a**–**c**) we consider cases with $N_a = 100, 116$, and 132 that correspond to $N_{QD} = 11, 13$, and 15, respectively. For $N_a = 116$ and $N_a = 132$, the lengths of SGQDs are 12.2 nm and 13.9 nm, respectively.
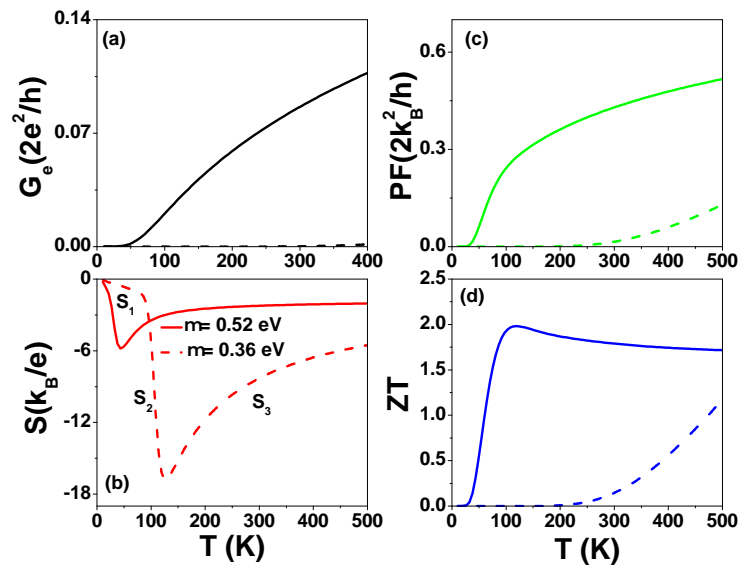

Figure 10. (**a**) Electrical conductance G_e, (**b**) Seebeck coefficient S, (**c**) power factor PF, and (**d**) figure of merit ZT of SGQD with $N_z = 5$ and $N_a = 132$ ($N_{QD} = 15$) as functions of temperature for different μ at $\Gamma_t = 2.7$ eV. The phonon thermal conductance (κ_{ph}) adopted is the same as in Figure 8.

Overall, we found no appreciable improvement in the power factor of t-AGNRs in comparison to AGNRs. Although electron Coulomb interactions are neglected in this calculation, our conclusion is still valid even in the Coulomb blockade regime. When the thermoelectric behavior of SGQDs is dominated by the TATP, electron–electron correlation functions are usually small [69]. Therefore, we can neglect electron Coulomb interactions when μ is inside the gap between two subbands.

4. Conclusions

We have theoretically investigated the transport and thermoelectric properties of SGQDs, which are formed by tailoring ZGNRs and AGNRs. Our calculations are based on Green's function approach within a tight-binding model. An electron-coherent tunneling process is found to be responsible for the electrical conductance spectra of SGQDs. The subband width and central gap of SGQDs can be modulated by varying the size of GQDs and inter-dot coupling strength. Unlike G_e and κ_e, Seebeck coefficients are found to be insensitive to the contact property between the SGQDs and electrodes. As a result, the power factor and thermoelectric figure of merit can be improved by modulating the tunneling rates. The maximum ZT values at room temperature occur when the chemical potential, μ, is close to the HOMO (LUMO) level in a typical situation where phonons dominate the heat transport. As shown in Figures 6 and A3, the maximum power factor (figure of merit) of t-ZGNRs at room temperature can reach 90% (95%) of the ideal situation with a square-form transmission coefficient. We also found that SGQDs based on t-ZGNRs can outperform SGQDs based on t-AGNRs for thermoelectric applications. The significantly improved thermoelectric behavior of the textured ZGNR is attributed to the sharp change in its transmission coefficient near the central gap. We found that defects at interior sites will not ruin the robust behavior of $\mathcal{T}_{LR}(\varepsilon)$ associated with the edge states near the LUMO of t-ZGNRs. This implies that the electron mean free path, λ_e, contributed by the zigzag edge states ($\lambda_{e,edge}$), can be much larger than the contribution from bulk states ($\lambda_{e,bulk}$). When the channel length (L_z) of t-ZGNRs is much larger than λ_{ph} and $\lambda_{e,bulk}$, κ_{ph} is seriously suppressed in such a diffusing region. The electronic states in the first miniband (near LUMO) of t-ZGNRs showing nonlinear dispersion could remain coherent due to their unique nature [27] (see Figure A2a). As a consequence, the power factor of Figure 6 remains valid; meanwhile, the corresponding ZT could be further enhanced [13]. At room temperature with $T = 324$ K ($k_B T = 27$ meV), the electrical power output can reach 0.212 nW/K for each SGQD implemented by using t-ZGNR. For an SGQD array with a density of 5×10^6 cm^{-1} and ZT larger than 3, the estimated power output is around mW/K, which can be applicable for low-power wearable electronic devices [70].

Author Contributions: D.M.T.K. initiated the idea and performed the calculation; D.M.T.K. and Y.-C.C. both contributed to the development of the computational code and carried out the data analyses; D.M.T.K. and Y.-C.C. wrote the manuscript. All authors have read and agreed to the published version of the manuscript.

Data Availability Statement: The data presented in this study are available upon reasonable request.

Conflicts of Interest: The authors declare no conflict of interest.

Appendix A

Appendix A.1. Charge Density of t-ZGNRs

To further clarify the electronic states shown in Figure 3, we plot the charge densities of $|\Psi_{\ell,j}(\varepsilon_{LU})|^2$, $|\Psi_{\ell,j}(\varepsilon_{e,1})|^2$, and $|\Psi_{\ell,j}(\varepsilon_{e,2})|^2$ for the 6-GQD case formed by t-ZGNRs with $N_a = 12$ and $N_z = 47$ in Figure A1, which correspond to the electronic states with energies

$\varepsilon_{LU} = 0.247$ eV, $\varepsilon_{e,1} = 0.3105$ eV, and $\varepsilon_{e,2} = 0.468$ eV in Figure 3f. As seen in Figure A1a, the charge density distribution in each GQD is the same for the electronic state with energy ε_{LU}. The maximum charge densities occur at sites labeled by $\ell = 1$ and $\ell = 12$ (along the bottom and top zigzag edges) and $j = 4 + 8\,m$, where m is an integer. At interior sites of each GQD, the charge density is very low. For $\varepsilon_{e,1} = 0.3105$ eV, the charge density at the central two GQDs is negligible. For $\varepsilon_{e,2} = 0.468$ eV, the charge density at the 2nd and 5th GQDs is dilute. For $\varepsilon_{e,6} = 1.0665$ eV, the charge density at the 1st and the 6th GQDs is smaller than those of other GQDs (not shown here). This indicates that the electronic states near $\varepsilon_{e,6} = 1.0665$ eV are weakly coupled to the electrodes. Based on the charge density distribution shown in Figure A1, the defect location-dependent behavior of G_e shown in Figure 4 can be clearly illustrated. The G_e is not degraded seriously when defects are located at sites with low charge density.
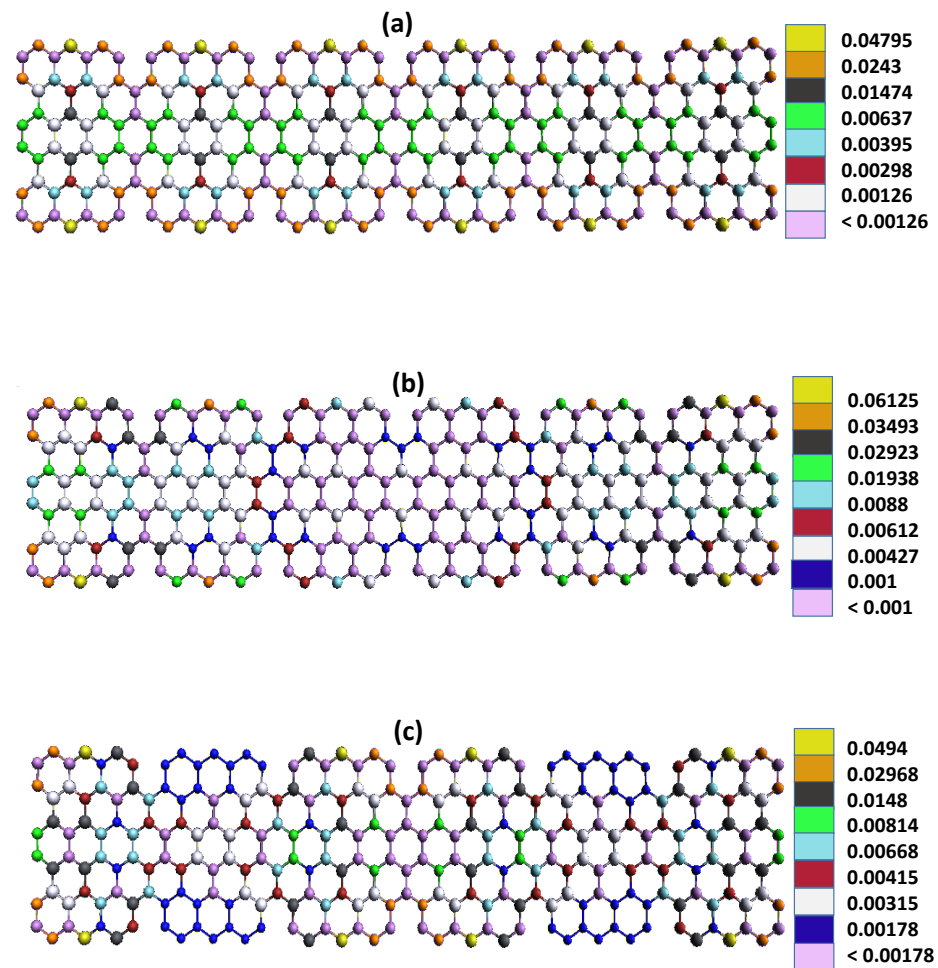

(a)

	0.04795
	0.0243
	0.01474
	0.00637
	0.00395
	0.00298
	0.00126
	< 0.00126

(b)

	0.06125
	0.03493
	0.02923
	0.01938
	0.0088
	0.00612
	0.00427
	0.001
	< 0.001

(c)

	0.0494
	0.02968
	0.0148
	0.00814
	0.00668
	0.00415
	0.00315
	0.00178
	< 0.00178

Figure A1. Charge density $|\Psi_{\ell,j}(\varepsilon)|^2$ for the t-ZGNR with conductance spectrum shown in Figure 3f. Diagrams (**a**–**c**) are the charge densities of $\varepsilon_{LU} = 0.247$ eV, $\varepsilon_{e,1} = 0.3105$ eV, and $\varepsilon_{e,2} = 0.468$ eV, respectively.

Appendix A.2. Electronic Band Structures

In Figure A2, we show comparisons of the subband structures of graphene nanoribbons with and without modification of the side edges. Here, the length of the unit cell in t-GNRs is denoted L. For the t-ZGNR with its unit cell characterized by $N_a = 8$ and $N_z = 8$, we have $L = 4a$, where a is the lattice constant of ZGNR. For the t-AGNR characterized by $N_z = 5$ and $N_a = 8$, we have $L = 2a'$, where $a' = \sqrt{3}a$ is the lattice constant of AGNR. We note that the first Brillouin zone (BZ) has one quarter (half) the size of the BZ of ZGNR (AGNR). Thus, the subband structures shown in Figure A1 include the zone-folding effect

that maps the zone boundary $k_z = \pi/a$ ($k_z = \pi/a'$) of the unfolded BZ of ZGNR (ANGR) to $k_z = 0$ of the folded BZ. Here, we show the electronic structure of $N_a = 8$ rather than $N_a = 12$ in Figure A2a. For $N_a = 8$, we observe not only the central gap, but also a gap between the first subband and the second subband.
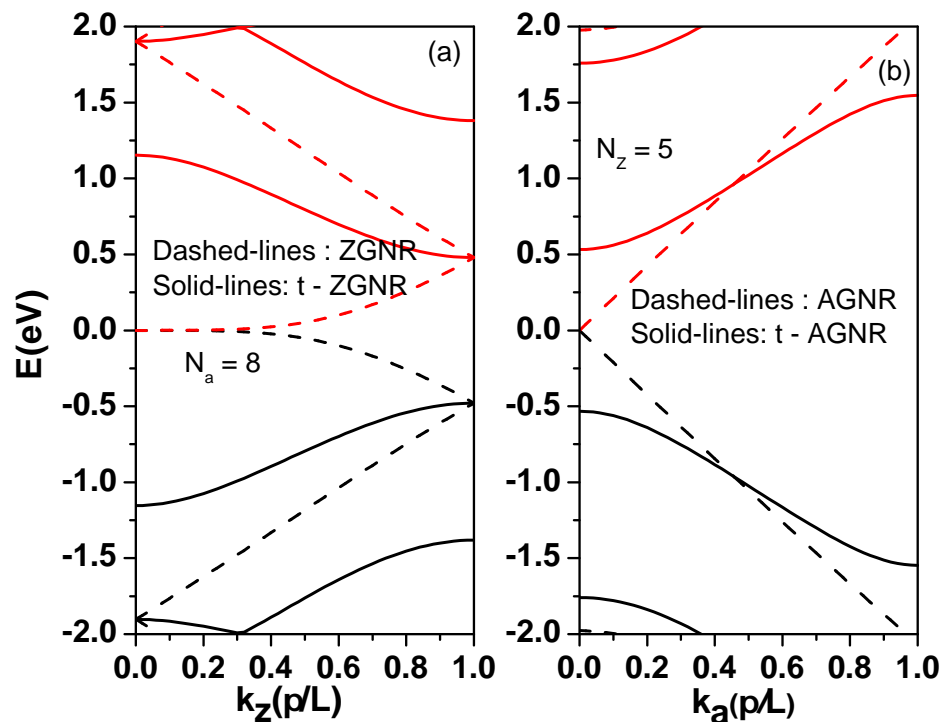

Figure A2. (**a**) Subband structures of t-ZGNR superlattice with a unit cell of length *L* characterized by $N_a = 8$ and $N_z = 8$ (solid lines) as depicted in Figure 1b, and corresponding ZGNR (without texture) of the same length of unit cell (dashed lines). (**b**) Subband structures of t-AGNR superlattice with a unit cell characterized by $N_z = 5$ and $N_a = 8$ (solid lines) as depicted in Figure 1d, and corresponding AGNR (without texture) of the same length of unit cell (dashed lines).

Appendix A.3. ZT Optimization of Textured ZGNRs

In Figure A3, we show the calculated $\mathcal{T}_{LR}(\varepsilon)$ in the region of $\varepsilon > 0$ for two types of t-ZGNRs: (a) with indentation on both zigzag sides and (b) with indentation on only one zigzag side of the t-ZGNR. Both t-ZGNRs consist of 15 GQDs (same as the one considered in Figures 5 and 6). The solid, dashed, dotted, and dot-dashed lines correspond to $\Gamma_t = 0.45, 0.54, 0.63$, and 0.72 eV, respectively. As energy ε is tuned away from LUMO, many sharp peaks appear in the spectrum as a consequence of the Fabry–Perot interference. The period of Fabry–Perot interference in (b) is larger than that in (a). When ε becomes close to *LUMO*, electronic states cannot be clearly resolved due to their nonlinear dispersion. Diagram (c) shows ZT_{max} of a t-ZGNR consisting of 15 GQDs as a function of the tunneling rate Γ_t at $k_B T = 27$ meV and $\mu = 0.423$ eV. It is found that ZT_{max} can be larger than 3 for Γ_t between 0.18 eV and 1.45 eV for the case of (a). When the barrier height becomes smaller, the miniband width becomes wider. This indicates that the electron inter-dot hopping strengths are enhanced. This is why ZT_{max} occurs at $\Gamma_t = 0.72$ eV in (b). Since the theoretical limit for an ideal SF transmission coefficient is $ZT_{max} = 3.95167$, the maximum ZT value of t-ZGNRs can reach 95% of the ideal case.
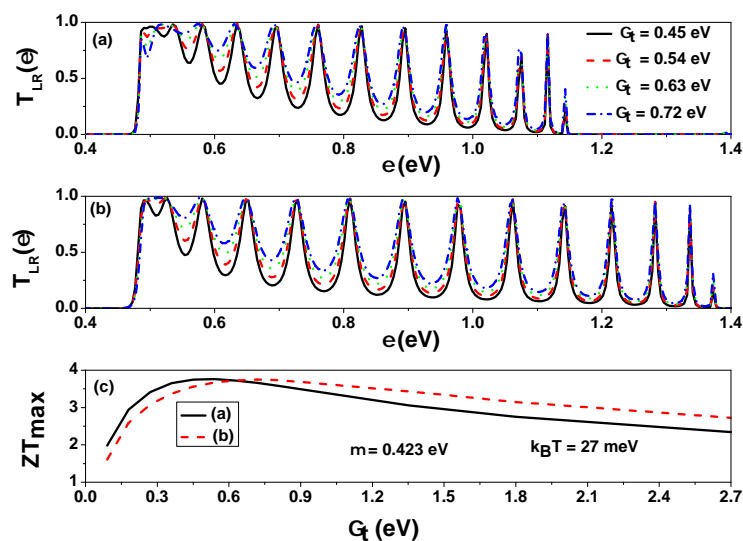
Figure A3. Transmission coefficient in the range of $\varepsilon > 0$ for different tunneling rates. (**a**) Periodically indented structures on both zigzag edge sides and (**b**) periodically indented structures on only one zigzag edge side. (**c**) ZT_{max} of a t-ZGNR consisting of 15 GQDs as a function of the tunneling rate Γ_t. Each GQD in the structure has size $N_a = 8$ and $N_z = 7$. The maximum ZT value of SF transmission coefficient at $k_B T = 27$ meV is 3.95167 when its κ_{ph} is adopted to be the same as that of Figure 5.

Appendix A.4. Local Density of States of Textured AGNRs

The $\mathcal{T}_{LR}(\varepsilon)$ spectrum cannot reveal the existence of zigzag edge states in a finite-size AGNR that decays exponentially along the armchair direction when the channel length is much longer than the decay length. These localized states of GNRs can be probed by STM [21]. In Figure A4, we show the calculated local density of states (LDOS) as a function of ε for various tunneling rates. Here, we define $LDOS = -Im(G^r_{\ell=2,j=1}(\varepsilon))/\pi$. The LDOS can reveal the existence of the zigzag edge states of an AGNR coupled to the electrodes. The zero-energy modes resulting from the outer zigzag edge structures of t-AGNRs are seen in Figure A4. Due to the localized nature of the zigzag edge states, the spectra in Figure 9 cannot reveal them. Meanwhile, these edge states localized at the interface are also strongly influenced by the variation in coupling strength between the electrodes and the t-AGNR. With increasing Γ_t, these zero-energy modes become broadened in (b) and (c).
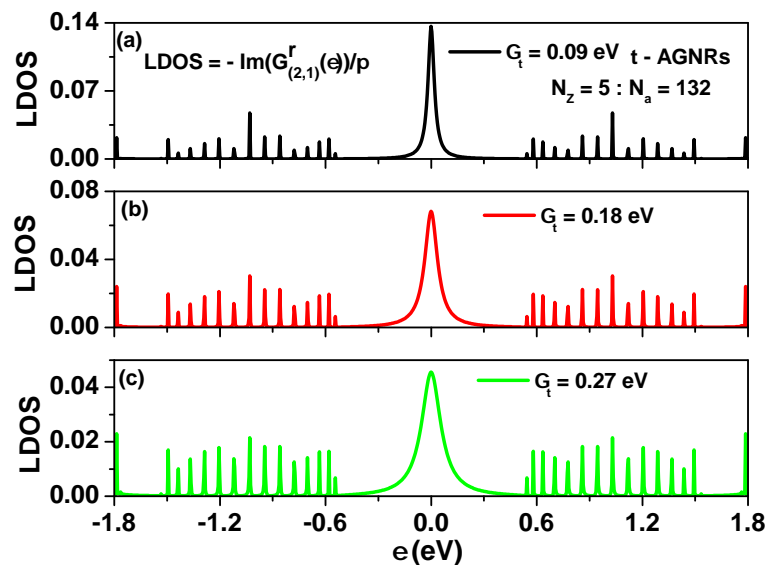

Figure A4. Local density of states of a t-AGNR with $(N_z, N_a) = (5,132)$ as a function of ε for various tunneling rates at site (2,1).

References

1. Chen, G.; Dresselhaus, M.S.; Dresselhaus, G.; Fleurial, J.P.; Caillat, T. Recent developments in thermoelectric materials. *Int. Mater. Rev.* **2003**, *48*, 45. [CrossRef]
2. Hicks L.D.; Dresselhaus, M.S. Thermoelectric figure of merit of a one-dimensional conductor. *Phys. Rev. B* **1993**, *47*, 16631. [CrossRef] [PubMed]
3. Hicks, L.D.; Dresselhaus, M.S. Effect of quantum-well structures on the thermoelectric figure of merit. *Phys. Rev. B* **1993**, *47*, 12727. [CrossRef] [PubMed]
4. Boukai, A.; Bunimovich, Y.; Tahir-Kheli, J.; Yu, J.K.; Goddard, W.A., III; Heath, J.R. Silicon nanowires as efficient thermoelectric materials. *Nature* **2008**, *451*, 168. [CrossRef]
5. Hochbaum, A.; Hochbaum, A.I.; Chen, R.; Delgado, R.D.; Liang, W.; Garmett, E.C.; Najarian, M.; Majumdar, A.; Yang, P.D. Enhanced thermoelectric performance of rough silicon nanowires. *Nature* **2008**, *451*, 163. [CrossRef]
6. Heremans, J.P.; Thrush, C.M.; Morelli, D.T.; Wu, M.C. Thermoelectric power of bismuth nanocomposites. *Phys. Rev. Lett.* **2002**, *88*, 216801. [CrossRef]
7. Nika, D.L.; Pokatilov, E.P.; Balandin, A.A.; Fomin, V.M.; Rastelli, A.; Schmidt, O.G. Reduction of lattice thermal conductivity in one-dimensional quantum-dot superlattices due to phonon filtering. *Phys. Rev. B* **2011**, *84*, 165415. [CrossRef]
8. Hu, M.; Poulikakos, D. Si/Ge Superlattice nanowires with ultralow thermal conductivity. *Nano Lett.* **2012**, *12*, 5487. [CrossRef]
9. Whitney, R.S. Most efficient quantum thermoelectric at finite power output. *Phys. Rev. Lett.* **2014**, *112*, 130601. [CrossRef]
10. Pietzonka, P.; Seifert, U. Universal trade-off between power, efficiency, and constancy in steady-state heat engines. *Phys. Rev. Lett.* **2018**, *120*, 190602. [CrossRef]
11. Chen, I.J.; Burke, A.; Svilans, A.; Linke, H.; Thelander, C. Thermoelectric power factor limit of a 1D nanowire. *Phys. Rev. Lett.* **2018**, *120*, 177703. [CrossRef]
12. Luo, R.X.; Benenti, G.; Casati, G.; Wang, J. Thermodynamic bound on heat-to-power conversion. *Phys. Rev. Lett.* **2018**, *121*, 080602. [CrossRef]
13. Xu, Y.; Gan, Z.; Zhang, S.C. Enhanced thermoelectric performance and anomalous Seebeck effects in topological insulators. *Phys. Rev. Lett.* **2014**, *112*, 226801. [CrossRef]
14. Darancet, P.; Olevano, V.; Mayou, D. Coherent electronic transport through graphene constrictions: Subwavelength regime and optical analogy. *Phys. Rev. Lett.* **2009**, *102*, 136803. [CrossRef]
15. Kagan, C.R.; Murry, C.B. Charge transport in strongly coupled quantum dot solids. *Nat. Nanotechnol.* **2015**, *10*, 1013. [CrossRef]
16. Lawrie, W.I.L.; Eenink, H.G.J.; Hendrickx, N.W.; Boter, J.M.; Petit, L.; Amitonov, S.V.; Lodari, M.; Paquelet Wuetz, B.; Volk, C.; Philips, S.G.J.; et al. Quantum dot arrays in silicon and germanium. *Appl. Phys. Lett.* **2020**, *116*, 080501. [CrossRef]
17. Novoselov, K.S.; Geim, A.K.; Morozov, S.V.; Jiang, D.; Zhang, Y.; Dubonos, S.V.; Grigorieva, I.V.; Firsov, A.A. Electric field effect in atomically thin carbon films. *Science* **2004**, *306*, 666. [CrossRef]
18. Cai, J.; Ruffieux, P.; Jaafar, R.; Bieri, M.; Braun, T.; Blankenburg, S.; Muoth, M.; Seitsonen, A.P.; Saleh, M.; Feng, X.; et al. Atomically precise bottom-up fabrication of graphene nanoribbons. *Nature* **2010**, *466*, 470. [CrossRef]
19. Chen, Y.C.; Cao, T.; Chen, C.; Pedramraz, Z.; Haberer, D.; de Oteyza, D.G.; Fischer, F.R.; Louie, S.G.; Crommie, M.F. Molecular bandgap engineering of bottom-up synthesized graphene nanoribbon heterojunctions. *Nat. Nanotechnol.* **2015**, *10*, 156. [CrossRef]
20. Groning, O.; Wang, S.; Yao, X.; Pignedoli, C.A.; Barin, G.B.; Daniels, C.; Cupo, A.; Meunier, V.; Feng, X.; Narita, A. Engineering of robust topological quantum phases in graphene nanoribbons. *Nature* **2018**, *560*, 209. [CrossRef]
21. Rizzo, D. J.; Veber, G.; Cao, T.; Bronner, C.; Chen, T.; Zhao, F.; Rodriguez, H.; Louie, S.G.; Crommie, M.F.; Fischer, F.R. Topological band engineering of graphene nanoribbons. *Nature* **2018**, *560*, 204. [CrossRef] [PubMed]
22. Yan, L.H.; Liljeroth, P. Engineered electronic states in atomically precise artificial lattices and graphene nanoribbons. *Adv. Phys. X* **2019**, *4*, 1651672. [CrossRef]
23. Rizzo, D.J.; Veber, G.; Jiang, J.W.; McCurdy, R.; Cao, T.; Bronner, C.; Chen, T.; Louie, Steven G.; Fischer, F.R.; Crommie, M.F. Inducing metallicity in graphene nanoribbons via zero-mode superlattices. *Science* **2020**, *369*, 1597. [CrossRef]
24. Sun, Q.; Yan, Y.; Yao, X.L.; Mullen, K.; Narita, A.; Fasel, R.; Ruffieux, P. Evolution of the topological energy band in graphene nanoribbons. *J. Phys. Chem. Lett.* **2021**, *12*, 8679. [CrossRef]
25. Rizzo, D.J.; Jiang, J.W.; Joshi, D.; Veber, G.; Bronner, C.; Durr, R.A.; Jacobse, P.H.; Cao, T.; Kalayjian, A.; Rodriguez, H.; et al. Rationally designed topological quantum dots in bottom-up graphene nanoribbons. *ACS Nano* **2021**, *15*, 20633. [CrossRef]
26. Llinas, J.P.; Fairbrother, A.; Borin Barin, G.; Shi, W.; Lee, K.; Wu, S.; Choi, B.Y.; Braganza, R.; Lear, J.; Kau, N.; et al. Short-channel field-effect transistors with 9-atom and 13-atom wide graphene nanoribbons. *Nat. Commun.* **2017**, *8*, 633. [CrossRef]
27. Lin, K.S.; Chou, M.Y. Topological properties of gapped graphene nanoribbons with spatial symmetries. *Nano Lett.* **2018**, *8*, 7254. [CrossRef]
28. Zuev, Y.M.; Chang, W.; Kim, P. Thermoelectric and magnetothermoelectric transport measurements of graphene. *Phys. Rev. Lett.* **2009**, *102*, 096807. [CrossRef]
29. Wei, P.; Bao, W.Z.; Pu, Y.; Lau, C.N.; Shi, J. Anomalous thermoelectric transport of Dirac particles in graphene. *Phys. Rev. Lett.* **2009**, *102*, 166808. [CrossRef]
30. Xu, Y.; Li, Z.Y.; Duan, W.H. Thermal and thermoelectric properties of graphene. *Small* **2014**, *10*, 2182. [CrossRef]
31. Wang, Y.H.; Yang, J.; Wang, L.Y.; Du, K.; Yin, Q.; Yin, Q.J. Polypyrrole/graphene/polyaniline ternary nanocomposite with high thermoelectric power factor. *ACS Appl. Mater. Interfaces* **2017**, *9*, 20124. [CrossRef] [PubMed]

32. Li, M.; Cortie, D.L.; Liu, J.X.; Yu, D.H.; Islam, S.M.K.N.; Zhao, L.L.; Mitchell, D.R.G.; Mole, R.A.; Cortie, M.B.; Dou, S.X. Ultra-high thermoelectric performance in graphene incorporated Cu2Se: Role of mismatching phonon modes. *Nano Energy* **2018**, *53*, 993. [CrossRef]

33. Ghosh, S.; Harish, S.; Ohtaki, M.; Saha, B.B. Thermoelectric figure of merit enhancement in cement composites with graphene and transition metal oxides. *Mater. Today Energy* **2020**, *18*, 100492. [CrossRef]

34. Wang Y.Y.; Chen D.R.; Wu J.K.; Wang T.H.; Chuang C.S.; Huang S. Y.; Hsieh W.P.; Hofmann M.; Chang Y.H.; Hsieh Y.P. Two-dimensional mechano-thermoelectric heterojunctions for self-powered Strain Sensors. *Nano Lett.* **2021**, *21*, 6990. [CrossRef]

35. He, J.; Tritt, T.M. Advances in thermoelectric materials research: Looking back and moving forward. *Science* **2017**, *357*, aak9997. [CrossRef]

36. Nakada, K.; Fujita, M.; Dresselhaus, G.; Dresselhaus, M.S. Edge state in graphene ribbons: Nanometer size effect and edge shape dependence. *Phys. Rev. B* **1996**, *54*, 17954. [CrossRef]

37. Wakabayashi, K.; Fujita, M.; Ajiki, H.; Sigrist, M. Electronic and magnetic properties of nanographite ribbons. *Phys. Rev. B* **1999**, *59*, 8271. [CrossRef]

38. Son, Y.W.; Cohen, M.L.; Louie, S.G. Half-metallic graphene nanoribbons. *Nature* **2006**, *444*, 347. [CrossRef]

39. Topsakal, M.; Sevincli, H.; Ciraci, S. Spin confinement in the superlattices of graphene ribbons. *Appl. Phys. Lett.* **2008**, *92*, 173118. [CrossRef]

40. Sevincli, H.; Topsakal, M.; Ciraci, S. Superlattice structures of graphene-based armchair nanoribbons. *Phys. Rev. B* **2008**, *78*, 245402. [CrossRef]

41. Haug, H.; Jauho, A.P. *Quantum Kinetics in Transport and Optics of Semiconductors*; Springer: Berlin/Heidelberg, Germany, 1996.

42. Kuo, D.M.T. Thermoelectric and electron heat rectification properties of quantum dot superlattice nanowire arrays. *AIP Adv.* **2020**, *10*, 045222. [CrossRef]

43. Phung, T.T.; Peters, R.; Honecker, A.; Trambly de Laissardiere, G.; Vahedi, J. Spin-caloritronic transport in hexagonal graphene nanoflakes. *Phys. Rev. B* **2020**, *102*, 035160. [CrossRef]

44. Chen, R.S.; Ding, G.L.; Zhou, Y.; Han, S.T. Fermi-level depinning of 2D transition metal dichalcogenide transistors. *J. Mater. Chem. C* **2021**, *9*, 11407. [CrossRef]

45. Mahan, G.D.; Woods, L.M. Multilayer thermionic refrigeration. *Phys. Rev. Lett.* **1998**, *80*, 4016. [CrossRef]

46. Chang, Y. C.; Schulman, J. N.; Bastard, G.; Guldner, Y. Effects of quasi-interface states in HgTe-CdTe superlattices. *Phys. Rev. B* **1985**, *31*, 2557. [CrossRef]

47. Bernevig, B.A.; Hughes, T.L.; Zhang, S.C. Quantum spin Hall effect and topological phase transition in HgTe quantum wells. *Science* **2006**, *314*, 1757. [CrossRef]

48. Kou, L.Z.; Wu, S.C.; Felser, C.; Frauenheim, T.; Chen, C.F.; Yan, B.H. Robust 2D topological insulators in van der Waals heterostructures. *ACS Nano* **2014**, *8*, 10448. [CrossRef]

49. Huang, H.Q.; Duan, W.H. Topological insulator quasi-1D topological insulators. *Nat. Mater.* **2016**, *15*, 129. [CrossRef]

50. Zhu, Z.L.; Cai, X.L.; Yi, S.H.; Chen, L.; Dai, Y.W.; Niu, C.Y.; Guo, Z.X.; Xie, M.H.; Liu, F.; Cho, J.H.; et al. Multivalency-driven formation of Te-based monolayer materials: A combined first-principles and experimental study. *Phys. Rev. Lett.* **2017**, *119*, 106101. [CrossRef]

51. Xian, L.; PerezPaz, A.; Bianco, E.; Ajayan, P.M.; Rubio, A. Square selenene and tellurene: Novel group VI elemental 2D materials with nontrivial topological properties. *2D Mater.* **2017**, *4*, 041003. [CrossRef]

52. Mahan, G.D.; Sofo, J.O. The best thermoelectric. *Proc. Natl. Acad. Sci. USA* **1996**, *93*, 7436. [CrossRef] [PubMed]

53. Chang, P.H.; Bahramy, M.S.; Nagaosa, N.; Nikolic, B.K. Giant thermoelectric effect in graphene-based yopological insulators with heavy adatoms and nanopores. *Nano Lett.* **2014**, *14*, 3779. [CrossRef]

54. Wakabayashi, K.; Sasaki, K.; Nakanishi, T.; Enoki, T. Electronic states of graphene nanoribbons and analytical solutions. *Sci. Technol. Adv. Mater.* **2010**, *11*, 054504. [CrossRef]

55. Areshkin, D.A.; Gunlycke, D.; White, C.T. Ballistic transport in graphene nanostrips in the presence of disorder: Importance of edge effects. *Nano Lett.* **2007**, *7*, 204. [CrossRef] [PubMed]

56. Martins, T.B.; da Silva, A.J.R.; Miwa, R.H.; Fazzio, A. sigma- and pi-defects at graphene nanoribbon edges: Building spin filters. *Nano Lett.* **2008**, *8*, 2293. [CrossRef]

57. Li, T.C.; Lu, S.P. Quantum conductance of graphene nanoribbons with edge defects. *Phys. Rev. B* **2008**, *77*, 085408. [CrossRef]

58. Shen, P.-C.; Su, C.; Lin, Y.; Chou, A.-S.; Cheng, C.-C.; Park, J.-H.; Chiu, M.-H.; Lu, A.-Y.; Tang, H.-L.; Tavakoli, M.M.; et al. Ultralow contact resistance between semimetal and monolayer semiconductors. *Nature* **2021**, *593*, 212. [CrossRef]

59. Zheng, H.; Liu, H.J.; Ta, X.J.; Lv, H.Y.; Pan, L.; Shi, J.; Tang, X.F. Enhanced thermoelectric performance of graphene nanoribbons. *Appl. Phys. Lett.* **2012**, *100*, 093104. [CrossRef]

60. Sevincli, H.; Cuniberti, G. Enhanced thermoelectric figure of merit in edge-disordered zigzag graphene nanoribbons. *Phys. Rev. B* **2010**, *81*, 113401. [CrossRef]

61. Murphy, P.G.; Moore, J.E. Coherent phonon scattering effects on thermal transport in thin semiconductor nanowires. *Phys. Rev. B* **2007**, *76*, 155313. [CrossRef]

62. Samuelsson, P.; Kheradsoud, S.; Sothmann, B. Optimal quantum interference thermoelectric heat engine with edge States. *Phys. Rev. Lett.* **2017**, *118*, 256801. [CrossRef]

63.   Mazzamuto, F.; Hung Nguyen, V.; Apertet, Y.; Caer, C.; Chassat, C.; Saint-Martin, J.; Dollfus, P. Enhanced thermoelectric properties in graphene nanoribbons by resonant tunneling of electrons. *Phys. Rev. B* **2011**, *83*, 235426. [CrossRef]

64.   Dollfus, P.; Nguyen, V.H.; Saint-Martin, J. Thermoelectric effects in graphene nanostructures. *J. Phys. Condens. Matter* **2015**, *27*, 133204. [CrossRef]

65.   Tran, V.T.; Saint-Martin, J.; Dollfus, P. High thermoelectric performance in graphene nanoribbons by graphene/BN interface engineering. *Nanotechnolgy* **2015**, *26*, 495202. [CrossRef]

66.   Merino-Diez, N.; Garcia-Lekue, A.; Carbonell-Sanroma, E.; Li, J.C.; Corso, M.; Colazzo, L.; Sedona, F.; Sanchez-Portal, D.; Pascual, J.I.; de Oteyza, D.G. Width-dependent band gap in armchair graphene nanoribbons reveals Fermi level pinning on Au(111). *ACS Nano* **2017**, *11*, 11661. [CrossRef]

67.   Lee, P.A.; Ramakrishnan, T.V. Disordered electronic systems. *Rev. Mod. Phys.* **1985**, *57*, 287. [CrossRef]

68.   Kuo, D.M.T.; Chang, Y.C. Thermoelectric and thermal rectification properties of quantum dot junctions. *Phys. Rev. B* **2010**, *81*, 205321. [CrossRef]

69.   Kuo, D.M.T.; Chen, C.C.; Chang, Y.C. Large enhancement in thermoelectric efficiency of quantum dot junctions due to increase of level degeneracy. *Phys. Rev. B* **2017**, *95*, 075432. [CrossRef]

70.   Suarez, F.; Nozariasbmarz, A.; Vashaee, D.; Ozturk, M.C. Designing thermoelectric generators for self-powered wearable electronics. *Energy Environ. Sci.* **2016**, *9*, 2099. [CrossRef]